

RESEARCH ARTICLE

10.1029/2017JG004273

Key Points:

- The effect of sea-level rise on methane emissions is incorporated into a methane model
- The effect of sea-level rise on methane emissions varies in different watersheds
- Sea-level rise is likely to increase inundation extent and CH₄ emissions under a warming climate

Supporting Information:

- Supporting Information S1

Correspondence to:

Y. Zhou,
yuyuzhou@iastate.edu

Citation:

Lu, X., Zhou, Y., Zhuang, Q., Prigent, C., Liu, Y., & Teuling, A. (2018). Increasing methane emissions from natural land ecosystems due to sea-level rise. *Journal of Geophysical Research: Biogeosciences*, 123. <https://doi.org/10.1029/2017JG004273>

Received 1 NOV 2017

Accepted 1 MAY 2018

Accepted article online 11 MAY 2018

Increasing Methane Emissions From Natural Land Ecosystems due to Sea-Level Rise

Xiaoliang Lu¹ , Yuyu Zhou² , Qianlai Zhuang³ , Catherine Prigent⁴ , Yaling Liu⁵, and Adriaan Teuling⁶ 

¹Department of Forest Ecosystems and Society, Oregon State University, Corvallis, OR, USA, ²Department of Geological and Atmospheric Sciences, Iowa State University of Science and Technology, Ames, IA, USA, ³Department of Earth, Atmospheric, and Planetary Sciences, Purdue University, West Lafayette, IN, USA, ⁴Laboratoire d'Etudes du Rayonnement et de la Matière en Astrophysique, CNRS, Observatoire de Paris, Paris, France, ⁵Pacific Northwest National Laboratory, Joint Global Change Research Institute, College Park, MD, USA, ⁶Hydrology and Quantitative Water Management Group, Wageningen University, Wageningen, Netherlands

Abstract Atmospheric methane (CH₄) is one of the most important greenhouse gases. However, there is still a large uncertainty in simulating CH₄ emissions from terrestrial ecosystems. Different from modeling studies focusing on response of CH₄ emissions to various environmental changes in land ecosystems, this study analyzed the response of CH₄ emissions to sea-level rise (SLR). To do so, a large-scale surface water routing module was incorporated into an existing CH₄ model. This allowed the model to simulate the effect of SLR on river flows and inland water levels. This study focused on these freshwater systems and did not address saltwater intrusion or coastal wetland impacts. Both the annual maximum inundation extent and CH₄ emissions at the global level showed a steadily growing trend, with an increase of 1.21×10^5 km² in extent and an increase of 3.13 Tg CH₄/year in CH₄ emissions, in a 22-year SLR experiment from 1993 to 2014. Most of new inundation and methane source areas were located near rivers' deltas and along downstream reaches of rivers. The increase in the inundation extent is primarily influenced by precipitation, channel geomorphic characteristics, and topography of riverside area. The increase of CH₄ emissions due to the SLR is largely determined by the inundation extent, but other factors such as air temperature and carbon storage also play roles. Although the current SLR-induced increases in the inundation extent and CH₄ emissions only accounted for 1.0% and 1.3% of their global totals, these increases contributed 7.0% and 17.3% of the mean annual variability in both, respectively, during the study period. Considering that SLR has a long-term increasing trend, future SLR under a changing climate could play a more important role in global CH₄ emissions.

1. Introduction

Methane (CH₄) is one of the most important greenhouse gases with around 22 times stronger radiative forcing than CO₂. Recent studies have shown that the recent warming trend may enhance CH₄ emissions (Eliseev et al., 2008; Ringeval et al., 2011). Therefore, it is important to quantify CH₄ emissions under a changing climate. Although many interacting factors such as soil temperature, vegetation type, and soil texture affect CH₄ emissions, flooded extent is one of the most important factors in controlling natural CH₄ emissions (Bohn et al., 2015; Melton et al., 2013). Typically, regional flooded extent is estimated in two ways: (1) water surface retrieved from satellite-borne active/passive sensors such as Global Inundation Extent from Multi-Satellites (GIEMS; Papa et al., 2010; Prigent et al., 2007) and the Surface Water Microwave Product Series (Schroeder et al., 2010, 2015) and (2) saturated areas simulated using hydrological models (Hopcroft et al., 2011; Lu et al., 2016; Lu & Zhuang, 2012) accounting for a variety of controlling factors including precipitation, soil temperature, topography variations, and vegetation coverage. However, to our knowledge, the impacts of ocean dynamics on terrestrial CH₄ emissions have not yet been evaluated.

The magnitude of sea-level rise (SLR) has accelerated since 1990 (Merrifield et al., 2009). The altimeter measurements indicated that global mean sea level has risen about 5.4 cm from 1993 to 2011 at a rate of approximately 3.3 mm/year (Church & White, 2006). SLR may cause wave overtopping, coast inundation, and hurricane storm surge, damaging coastal roads and communities (Nicholls & Cazenave, 2010). SLR affects inundation in two ways. First, rising sea levels can directly inundate coastal areas with seawater. Second, SLR indirectly increases inland freshwater inundation area by reducing the hydraulic gradient from rivers

to the ocean. This study focuses on the freshwater inundation effect. Physically, the rivers' outflow to ocean is determined by the difference of water surface elevation between river and sea level at rivers' outlets. Increasing sea level may reduce hydraulic gradient, decreasing outflows from river to ocean and even seawater invasion in some regions. The decreased outflows in turn will increase the inundated extent in basins' upstream areas. For example, Yamazaki, Baugh, et al. (2012) found that the ocean tide can increase the inundated area in the upstream region of the Amazon River basin as far as 800 km from the river outlet. On the other hand, it is well known that the extent of inundated area is positively related to CH₄ emissions (Melton et al., 2013). Thus, SLR is expected to increase CH₄ emissions.

The response of global CH₄ emission to SLR is yet poorly understood. Virtually all current CH₄ models lack the ability to simulate effects of SLR on CH₄ emissions. There are two reasons. First, a surface water transport module is missing in almost all current CH₄ models. River outflow is linked to the dynamics of inundated extent through surface water movement: surface lateral flows bring runoff generated in uplands to lowlands, river, and eventually oceans. Unfortunately, recent CH₄ model intercomparison studies (WETCHIMP; Bohn et al., 2015; Melton et al., 2013) indicated that no CH₄ model can simulate surface lateral flow of water and its impacts on methane emissions. Without accounting for effects of surface water movement on inundation extent may lead to obvious underestimation of inundated areas (Lu et al., 2016). Further, the response of inundated area to SLR cannot be addressed in those models due to no mechanism considering surface water transport from ground surface to oceans. In contrast, the incorporation of a water routing module should not only significantly improve estimation of inundated area (Lu et al., 2016) but also link between inundated areas and ocean dynamics.

This study improved our existing CH₄ model by adding a large-scale water routing module and taking a new way to allow the coarse-resolution model effectively capture small variations in the inundated areas. By using this improved modeling framework, we simulated the change of inundation extent due to the SLR during 1993–2014 and analyzed its effects on the regional and global CH₄ emissions. We are aware that CH₄ emissions may also occur from areas inundated by seawater. However, due to lacking sufficient data and limited understanding of biogeochemical processes for CH₄ production in saline wetlands, this mechanism was not yet included in our global CH₄ model. (See Text S4 in the supporting information for their difference.)

2. Methods

2.1. The CH₄ Model

Our methane modeling framework is built on our previous work (Zhuang et al., 2004). In the previous model, CH₄ production (methanogenesis) is assumed to only occur in the saturated zone and oxidation (methanotrophy) in the unsaturated zone; CH₄ is released into the atmosphere through three different pathways including diffusion, plant-aided transport, and ebullition. The effects of climate, carbon substrate availability (net primary production is used as the proxy), vegetation type, rooting depth, soil texture, soil pH, and redox potentials on methanogenesis and methanotrophy processes are considered. The hydrological module is modified from the terrestrial ecosystem model (Melillo et al., 1993; Zhuang et al., 2003). Lu and Zhuang (2012) replaced the original hydrology component with the variable infiltration capacity (VIC) model (Cherkauer & Lettenmaier, 1999; Cherkauer et al., 2003; Liang et al., 1994), a large-scale hydrological model, and also improved the methane module in three aspects. First, the TOPMODEL-based formulation is used to represent subgrid variability in the soil moisture distribution (Beven & Kirkby, 1979). Second, the effects of freeze and thaw cycles are also considered by coupling VIC simulation results. Third, methane ebullition is modeled as a function of pressure and soil temperature. The inundation extent in Lu and Zhuang (2012) is determined by soil moisture estimated from VIC simulation and local topographic information using a topographic wetness index in the TOPMODEL-based formulation. Soil moisture is higher in lowland areas as indicated by topographic wetness index compared to uplands. Many current CH₄ models also use this similar TOPMODEL-based approach to capture the subgrid heterogeneity in moisture distribution (Bohn et al., 2007; Ringeval et al., 2011, 2012). However, water can also flow along with topographic gradient and all grid points through the transport pathway could be inundated. Therefore, the inundation extent due to water contribution from upstream areas could be large in some watersheds (Kim et al., 2009). However, the contribution of water lateral flow was not considered in the TOPMODEL-based scheme; thus, the SLR effects on the change of inundation extent were missing.

2.2. A New Inundation Extent Module

To capture the effects of the surface water dynamics in the CH₄ model, a surface water routing model is needed to track the movement of surface runoff. In this study, the Catchment-based Macro-scale Floodplain (CaMa-Flood) model (Yamazaki et al., 2011; Yamazaki, Baugh, et al., 2012; Yamazaki, Lee, et al., 2012) was incorporated into our CH₄ model to simulate the effect of SLR on the hydrodynamics (Lu et al., 2016). The CaMa-Flood model is a large-scale routing model, which takes surface runoff generated from land surface models (VIC in this study) as an input and simulates the change of surface water storage in river networks and floodplains. In the CaMa-Flood model, the high-resolution topography information is used to derive the channels and floodplain elevation function relates floodplain depth to flooded area (Yamazaki et al., 2009). River discharge from upstream grid points to downstream points is largely regulated by water surface gradient. At river outlets, sea level is treated as the boundary condition for the diffusive wave equation (Bates et al., 2010) and is set to zero in most cases when SLR is not considered.

In our new inundation extent module, the inundation extent (I) is the saturated zone that is determined by two processes: (1) local water balance and topography, which have been implemented in our previous framework by using the TOPMODEL-based approach, and (2) uplands runoff, which is implemented in this study. The VIC and CaMa-Flood models were applied at 1° and 1/4° spatial resolutions, respectively. In the first process, the 1° resolution soil moisture was redistributed to finer 0.25° resolution grids and inundation extent generated in the first process was denoted as $I_{VIC + Topmodel}$. In the second process, surface runoff from the VIC simulation was assigned to CaMa-Flood grids (0.25°) using a nearest-point interpolation. The key information used in the CaMa-Flood model such as channel networks, channel depth, channel width, and flow direction was generated from a high-resolution topographic data set (Yamazaki et al., 2009, 2014). Water is assumed to instantaneously exchange between channels and floodplain; thus, water surface elevation is the same in these two reservoirs. The inundation extent generated by the second process is denoted as $I_{VIC + CaMa - Flood}$. The inundation extent, I , used in the further analysis is the union (U) of $I_{VIC + Topmodel}$ and $I_{VIC + CaMa - Flood}$:

$$I = U [I_{VIC+Topmodel}, I_{VIC+CaMa-Flood}] \quad (1)$$

I is essentially determined by three factors: (1) local soil moisture and heterogeneous topographic information ($I_{VIC + Topmodel}$), (2) runoff generated from local grid cells and upland areas ($I_{VIC + CaMa - Flood}$), and (3) water surface elevation in river channels and floodplain ($I_{VIC + CaMa - Flood}$). Water surface in rivers is directly affected by the sea level at their outlets. A water balance module (i.e., $I_{VIC + Topmodel}$ in equation (1)) that is used in most traditional inundation models is able to estimate inundated areas caused by saturation excess runoff. However, a large fraction of “small” and “short-term” inundated areas could be caused by infiltration excess runoff (Lu et al., 2016). In this situation, soil may be still unsaturated. The incorporation of the water surface routing module (i.e., $I_{VIC + CaMa - Flood}$ in equation (1)) provides an approach to estimate these inundated areas caused by these two processes.

It is important to note that increase in inundation extent due to SLR is usually much smaller compared to the typical resolution used in current large-scale CH₄ models. $I_{VIC + Topmodel}$ is a binary variable: inundated or not inundated. $I_{VIC + CaMa - Flood}$, however, can describe grid cells' inundation fraction at each time step. The minimum inundation extent is determined by the spatial resolution used in $I_{VIC + CaMa - Flood}$. The incorporation of $I_{VIC + CaMa - Flood}$ can significantly improve model's capability to simulate small variations in the inundation extent considering the impacts of sea level rise on the inundation extent in land.

2.3. The Response of CH₄ Emissions to SLR

In our previous methane module (Lu & Zhuang, 2012), grid cells are assigned inundation flags according to results from the TOPMODEL-based water table redistribution such as $I_{VIC + Topmodel}$. Each grid cell is either inundated or not inundated. Accordingly, methane production, oxidation, and transport processes are then simulated under either saturated ($I_{VIC + Topmodel} = 1$) or unsaturated ($I_{VIC + Topmodel} = 0$) conditions. After incorporating the CaMa-Flood model, each grid cell can have its inundation fraction (I), varying in the range between 0.0 and 1.0. A specific 0.25° grid cell with the area of A (m²) has CH₄ emissions (E , g CH₄/day) as described below:

$$E = F1 * A * (1 - I) + F2 * A * I \quad (2)$$

where F_1 ($\text{g CH}_4/\text{m}^2/\text{day}$) is methane flux which is estimated by the CH_4 model. To account for the inundation fraction provided by $I_{\text{VIC} + \text{CaMa} - \text{Flood}}$, we set up the other methane simulation (see Text S5 in the supporting information for the detailed explanation) in which soil column is saturated and its methane flux is estimated as F_2 . Methane emissions for the unsaturated part ($A * (1 - I)$) whose water table is still from the TOPMODEL-based water table redistribution is estimated as F_1 .

Using equation (2), the methane emissions are estimated according to the inundation fraction, which shall be more accurate than previous estimates at 0.25° resolution because I can vary continuously in the range between 0 and 1. Here we assume that the soil column below inundated zones is always saturated, which may introduce biases for a short-time simulation (seconds or minutes), while a daily time step used in this study can reduce the biases. In addition, possible infiltration process of overland flow is not considered in this study, which might also bias our analysis. More details are provided in the supporting information for the estimation of water table (Text S1) and CH_4 emissions (Text S2).

3. Input Data and Model Settings

The VIC model is used to generate the global 1° daily runoff from 1992 to 2014, which is in turn used as the input for the CaMa-Flood model and the methane module. The input data for the VIC model including gridded daily precipitation, maximum and minimum temperature, and wind speed were acquired from the National Centers for Environmental Prediction atmospheric reanalysis (Kalnay et al., 1996). Soil hydraulic parameters (Nijssen et al., 2001) and other vegetation parameters such as minimum stomatal resistance, albedo, rooting depth, and fraction specified for each vegetation class were obtained from the VIC model website (<http://www.hydro.washington.edu/Lettenmaier/Models/VIC/>). The land cover map was obtained from the University of Maryland's 1-km Global Land Cover product (Hansen et al., 2000) and processed as vegetation fraction data at a 1° resolution. In addition to soil moisture and temperature which are provided by the VIC simulation, the methane module also requires soil texture (Zhuang et al., 2003), soil-water pH (Carter & Scholes, 2000), vegetation type (Melillo et al., 1993), and the daily net primary production (NPP) which was generated from the Moderate Resolution Imaging Spectroradiometer (MODIS) 8-day NPP product (Running & Zhao, 2015) by assuming NPP to be the same within 1 month.

The CaMa-Flood model was implemented from 1992 to 2014. The first year, 1992, was used as a spin-up period and excluded from further analysis (Yamazaki et al., 2011). The input runoff at a 0.25° resolution used in the CaMa-Flood model was derived from 1° VIC simulations using a nearest neighbor interpolation. The required input data for the CaMa-Flood model include downstream cells, downstream distance, floodplain elevation profile, and global rivers' channel width, depth, and length, which are distributed with the model package.

The CaMa-Flood model uses the diffusive wave to model the water transport in river channels: water surface slope is the main factor in controlling discharge from one grid to its downstream grid. In river outlets, water surface slope is determined by water surface elevation and sea level. We set up two experiments to isolate the effect of the SLR on inundation extent: (1) sea level is set to zero for the whole simulation period, and land inundation extent is termed as $I_{\text{no sea}}$, and (2) sea level annually increases by 3.3 mm/year at all the rivers' outlets during 1993–2014 and the resulting inundation extent is named as I_{sea} .

4. Results and Discussion

4.1. Evaluation of Simulated Inundation Extent and Regional Methane Emissions

The simulated flooded extent was compared with GIEMS data (Papa et al., 2010; Prigent et al., 2007), which combined optical, passive, and active microwave sensors to build the global monthly inundated extent data set at a 25-km resolution from 1993 to 2007. The time series of global floodplains from the simulation (I) and the satellite observation are consistent regarding the seasonal pattern (Figure 1). The simulated inundation extent is larger than that from the multisatellite observation. The GIEMS data reported that the mean annual maximum inundation extent (MIE) is $5.61 \times 10^6 \text{ km}^2$ during the study period, while our estimation is close to $7.2 \pm 0.8 \times 10^6 \text{ km}^2$. The lower estimation of inundation extent from the satellite observations is mainly due to the low sensitivity of the retrieval algorithm in detecting small flooded areas (Prigent et al., 2007; Yamazaki et al., 2011). We also compared the simulated mean annual maximal inundation extent to that provided by eight hydrological models in the WETCHIMP (Table S1) including CLM4Me (Riley et al., 2011), DLEM (Tian

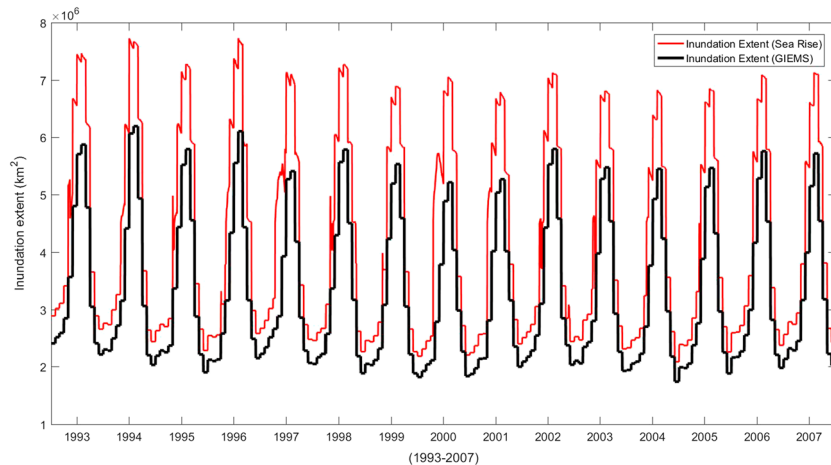


Figure 1. Global daily inundation extent estimated from Global Inundation Extent from Multisatellites (GIEMS, black line) and this study (red line) during 1993–2007. Note that the original time resolution of the satellite observations is monthly.

et al., 2011; Xu & Tian, 2012), LPJ-Bern (Spahni et al., 2011), LPJWHyMe (Wania et al., 2010), LPJ-WSL (Hodson et al., 2011), ORCHIDEE (Ringeval et al., 2011, 2012), SDGVM (Hopcroft et al., 2011; Singarayer et al., 2011), and UVic-ESCM (Avis et al., 2011). These models use the different assumptions and algorithms to estimate inundation distribution, and their simulation periods are also different; all these factors make it difficult to quantitatively compare them. However, our mean annual maximal inundation extent is comparable to their results.

Although we evaluated the methane module at the site level in the previous study (Lu & Zhuang, 2012), it is more meaningful to test the benefit of incorporating the surface water routing on a large scale. Airborne-based CH₄ observations are available in some regions, which are compared with our simulations. For instance, the annual CH₄ emissions were observed by aircrafts for the Hudson Bay lowland (Pickett-Heaps et al., 2011; Worthy et al., 2000) during the period 2004–2008 (Table S2). The previous studies reported Hudson Bay lowland as a methane source with a magnitude of 2.9–11.3 Tg CH₄/year (Table S2), which are comparable to our estimates (I_{new}) of 10.4 ± 1.3 Tg CH₄/year although our simulations are for a different period (Table S2). By upscaling the in situ chamber measurements, the previous estimated emissions are 3.92 ± 1.29 Tg CH₄/year from the West Siberian Lowlands (Glagolev et al., 2011; Winderlich et al., 2010) during 1993–2004, which is lower than our estimates of 8.74 Tg CH₄/year for the same period, using our earlier methane model (Bohn et al., 2015). Our new approach to estimating inundation extent (I) in this study provided a higher estimate of 11.7 Tg CH₄/year over the period of 2006–2010.

4.2. The Impact of SLR on Inundation Extent

Due to the 22-year SLR, the rate of increase ($I_{\text{sea}} - I_{\text{no sea}}$) in the annual MIE increased up to 1.21×10^5 km² on a global scale (Table 1). Temporally, we found that the annual MIE was larger at the beginning of the study period with an increase of 4.64×10^4 km² at the first 5 years of the study period, accounting for 38.3% of the total increase. Among the continents, Asia and North America gained the largest increases in their annual MIE by 4.2×10^4 and 3.1×10^4 km², contributing 35% and 26% of the total growth, respectively. In contrast, Africa and Oceania had the smallest increases in their annual MIE, increased by 7,314 and 5,607 km² or 0.01% and less than 0.01%, respectively (Table 1).

Over the same study period, the rate of increase ($I_{\text{sea}} - I_{\text{no sea}}$) in the daily MIE increased up to 5.62×10^4 km² globally (Figure 2a). Although the SLR-induced inundation extent was a small proportion (1.0%) of the global mean daily MIE ($7.2 \pm 0.8 \times 10^6$ km²) during the study period, it accounted for 7.0% of its variability (0.8×10^6 km²). Similar to the trend of the annual MIE, the daily MIE showed a larger increase at the beginning of the study period. The daily MIE increased more than 3.50×10^4 km² during the period of 1993–1999, while it increased with a slower rate of 2.00×10^4 km² in the remaining 15 years (Figure 1). Seasonally, the SLR tended to increase the flooded area more in spring (March–May) and winter (December–February) than in

Table 1

The Increase in the Annual Maximum Inundation Extent (km²) in the Continents due to the Sea-Level Rise During 1993–2014

Continents	1993	1994–1998	1999–2003	2004–2008	2009–2013	2014
South American	2,062.8	6,210.7	12,097.2	16,585.7	18,686.6	19,477.1
Europe	1,900.7	4,752.2	8,236.1	9,566.9	11,871.9	15,098.8
Asia	4,903.9	15,516.5	26,963.6	32,965.4	37,104.3	42,106.0
North America	4,286.9	13,574.5	21,457.2	26,192.7	29,466.3	31,204.8
Africa	1,211.0	3,644.0	5,550.9	6,407.7	7,073.4	7,314.9
Oceania	1,124.4	2,692.6	4,533.8	5,594.5	5,177.4	5,607.5
Global	15,489.6	46,390.4	78,838.8	97,312.9	109,379.9	120,809.1

Note. The values for 1994–1998, 1999–2003, 2004–2008, and 2009–2013 are the mean for the corresponding 5-year period.

summer (June–August; Figure 2a). The reason is that global inundation extent reached its peak in summer when SLR caused a deeper flood depth rather than more inundated areas. However, the expansion of inundation extent due to SLR is typically more pronounced in the early spring and winter.

In addition to inundation extent, duration of flood is also important in influencing methane emissions. By using 80% of mean daily MIE ($I_{no\ sea}$) estimated from each 0.25° grid cell in each continent during 1993–2014 as a threshold, we defined the duration of flood as the number of days in 1 year when each continent had inundated area larger than its threshold. Overall, the SLR extended the mean flood duration at the global level for 7 days and all the continents showed a longer flood duration (Figure 2b). The mean flood duration in South America, for example, was 94 days under no SLR simulation, while the SLR extended the flood duration by 3 days more (Figure 2b). Among the continents, Africa and Oceania extended their duration of flood most, which increased by 17 and 23 days, respectively (Figure 2b).

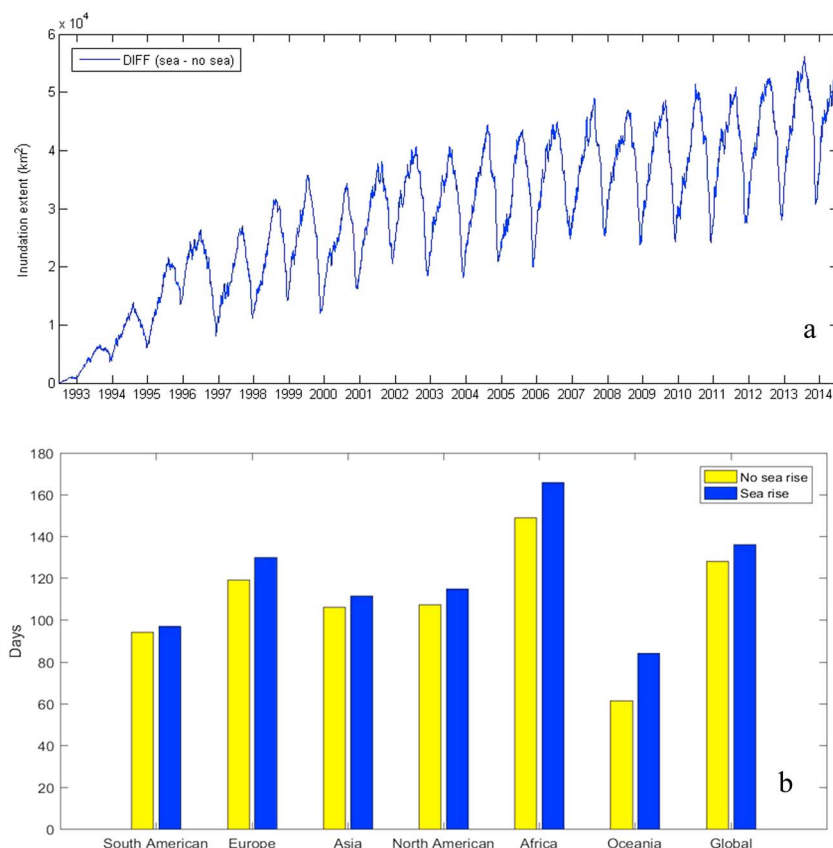


Figure 2. (a) Increases in the daily maximum inundation extent (km²). Ticks on the horizontal axis show June of each year and (b) the continent-level flood duration (days) due to the sea-level rise during 1993–2014.

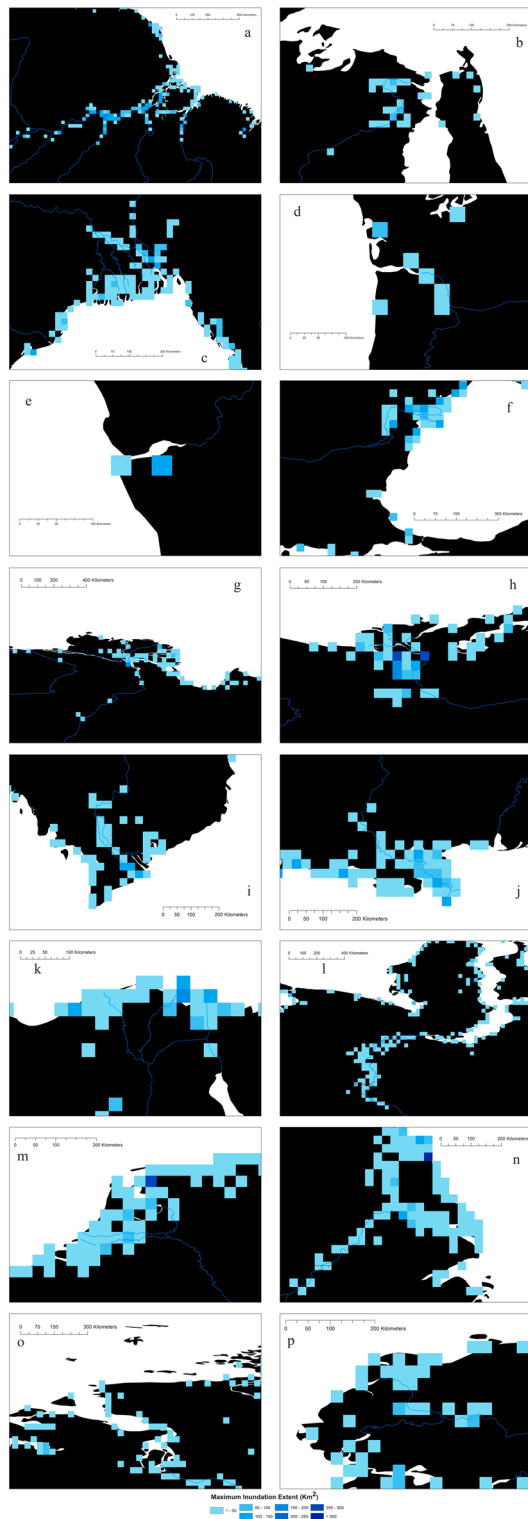


Figure 3. The increase in the annual maximum inundation extent (km^2) in 2014 due to sea-level rise in the selected major river basins: Amazon River (a), Amur River (b), Brahmaputra and Irrawaddy Rivers (c), Columbia River (d), Congo River (e), Danube River (f), Lena River (g), Mackenzie River (h), Mekong River (i), Mississippi River (j), Nile River (k), Ob River (l), Rhine River (m), Yangtze River (n), Yenisei River (o), and Yukon River (p). Pixels with more than 1 km^2 increase in the inundation extent are shown.

The extent of inundated areas in major river basins responded to the SLR differently. In some basins such as the Amazon River basin, the inundated area even increased in the upstream areas far away from the outlets, while other basins such as the Columbia River basin showed a slight growth in its inundation extent (Figure 3). We selected 16 major river basins across the globe and analyzed the factors affecting their responses to the SLR (Figure 3). At the watershed scale, large basins usually gained more inundation extent from SLR due to their large drainage area. For instance, the Amazon River basin, which has the largest basin area ($7.50 \times 10^6 \text{ km}^2$) among them, gained $13,135 \text{ km}^2$ more inundated area in 2014 after the 22-year SLR (Table 2). In contrast, the Rhine River basin with a small area of $0.19 \times 10^6 \text{ km}^2$ showed a $2,300 \text{ km}^2$ -increase in its inundation extent (Table 2). At the same time, inundated areas in some large basins, such as the Congo and Nile River basin, showed a relatively small response to the SLR (Table 2).

Different responses of these basins to the SLR indicate that factors other than basin area also play their roles. Specifically, we found that the development of inundation extent in a basin under SLR is determined by three factors. The first one is the relationship between maximum river depth and bank height (Table 3). In fact, this relationship reflects the interaction between geomorphologic factors and climate conditions: floods will not occur if maximum river depth is lower than bank height. In this case, water is always in river channels such that SLR cannot cause an increase in inundated areas. Among all the selected rivers, only the Congo River's bank height was always higher than its maximum river depth during 1993–2014 (Table 3). This suggested that the SLR should have a small effect on the inundation extent in the Congo River basin during that period. Although the Congo River basin has a large area of $4.01 \times 10^4 \text{ km}^2$, our simulation showed that it only increased by about 300 km^2 in its flooded area due to the SLR (Table 2). As expected, we found that the main river channel of the Congo River showed no increase in its inundated area and most of this 300-km^2 increase occurred in tributaries in its basin (Figure 3e).

The second factor is riverbed slope (see Text S6 in the supporting information): a flatter riverbed slope means that farther areas from outlets can be potentially flooded due to SLR. The Columbia and Congo Rivers have the steepest riverbed slopes (Table 3), suggesting that the expansion of inundation extent tends to be confined to places close to their outlets. Our simulations showed that both gained limited increases in their flooded area. The Columbia River basin, for example, only gained a small increase of 56 km^2 in its inundated areas (Table 2). Also, most of increases in their inundated areas occurred in downstream areas near their river deltas (Figures 3d and 3e). In contrast, the Amazon, Ob, and Yangtze rivers, however, have flat riverbeds (Table 3). Subsequently, the SLR increased the inundation extent in their upstream areas far away from their outlets by a magnitude even more than 500 km (Figures 3a, 3l, and 3n).

The third factor is floodplain elevation profile (see Text S6 in the supporting information), which describes floodplain water depth as a

Table 2

Annual and 5-Year Increase in the Maximum Inundation Extent (km²) due to the Sea-Level Rise in the Selected Basins During 1993–2014

Basins	Basin area (10 ⁶ km ²)	1993	1994–1998	1999–2003	2004–2008	2009–2013	2014
Amazon	7.50	954.7	3,320.3	8,270.8	11,154.5	12,478.3	13,135.7
Amur	1.86	46.1	528.7	1,432.5	1,916.1	1,897.0	2,198.5
Brahmaputra	0.71	72.0	328.6	629.1	1,061.5	1,101.7	1,516.6
Irrawaddy	0.41	157.7	293.0	419.6	440.7	509.6	582.6
Columbia	0.67	0.7	11.2	32.7	57.8	53.4	56.1
Congo	4.01	0.0	29.7	164.3	228.8	289.5	312.6
Danube	0.82	0.3	1.4	119.3	14.9	151.8	868.2
Lena	2.50	19.3	204.1	406.3	511.0	625.7	705.2
Mackenzie	1.81	31.4	192.2	492.2	687.8	1,015.9	1,165.8
Mekong	0.80	11.2	65.5	173.5	284.7	335.2	395.6
Mississippi	2.98	30.8	211.2	299.8	373.5	554.4	416.4
Nile	3.40	93.4	304.0	346.7	382.9	406.6	427.5
Ob	2.97	154.4	1,130.2	2,471.4	3,517.7	3,626.1	4,144.2
Rhine	0.19	258.1	684.7	1,060.6	1,191.4	1,550.5	2,309.2
Yangtze	1.81	8.8	234.5	572.6	922.6	1,154.7	1,151.8
Yenisei	2.58	102.8	337.0	804.8	1,193.6	1,316.2	1,606.0
Yukon	0.85	35.8	157.6	374.5	598.6	745.9	900.1
Global	NA	15,489.6	46,390.4	78,878.8	97,412.9	109,479.9	120,939.1

Note. NA = not applicable.

function of flooded area (Yamazaki et al., 2011). Flatter profile means more inundated area with the same amount of overland water. Combining above two factors of riverbed slope and floodplain elevation profile, the SLR showed the smallest effect on inundation extent in the Columbia and Congo River basins. Although the Amur River, for example, has the second smallest riverbed slope, its steep floodplain gradient (Tables 1 and 4) reduced the effect of the SLR on its inundation extent. Our simulations confirmed that the Amur River basin did obtain a large increase in its inundation extent, while most of them occurred in areas only about 10 km upstream from the outlet (Figure 3b).

4.3. The Impact of SLR on CH₄ Emissions

Roughly following the spatial distribution of growth in inundation extent, new source areas of CH₄ emissions due to the SLR were mainly located in places along downstream reaches of major rivers, especially in the

Table 3

The Maximum River Depths (m) With and Without the Effect of the Sea-Level Rise During 1993–2014, Bank Heights (m), Riverbed Slope, and Floodplain Gradient in the Selected Major Rivers

Rivers	Maximum river depth (no sea-level rise)	Maximum river depth (sea-level rise)	Bank height	Riverbed slope (10 ⁻⁶)	Floodplain gradient
Amazon	24.07	24.08	23.93	2.66	0.0035
Amur	15.80	15.80	8.62	3.51	0.0215
Brahmaputra	18.55	18.56	12.40	38.01	0.0005
Irrawaddy	9.82	9.82	9.66	36.42	0.0011
Columbia	15.49	15.50	6.10	112.15	0.0469
Congo	9.85	9.96	13.98	495.61	0.0119
Danube	8.34	8.35	6.68	18.94	0.0061
Lena	19.15	19.15	13.88	57.54	0.0154
Mackenzie	14.51	14.51	10.93	67.79	0.0033
Mekong	12.61	12.61	10.60	13.96	0.0005
Mississippi	13.41	13.42	10.72	20.39	0.0020
Nile	9.44	9.44	7.41	59.13	0.0073
Ob	15.89	15.90	13.52	10.09	0.0055
Rhine	5.59	5.59	4.02	58.41	0.0042
Yangtze	16.73	16.73	10.92	4.47	0.0084
Yenisei	23.89	23.89	12.98	13.21	0.0057
Yukon	17.42	17.42	8.49	8.76	0.0055

Note. The values are the mean for the 10 upstream grid cells from the river outlets.

Table 4
The Increase in CH₄ Emissions in the Continents (Tg CH₄/year) due to the Sea-Level Rise During 1993–2014

Continents	1993	1994–1998	1999–2003	2004–2008	2009–2013	2014
South American	0.3129	0.3366	0.4413	0.4852	0.5056	0.5271
Europe	0.2047	0.2864	0.3260	0.3702	0.3933	0.4129
Asia	0.4880	0.6207	0.8287	0.9732	1.0492	1.1319
North America	0.1984	0.1939	0.2170	0.3594	0.3612	0.3501
Africa	0.1977	0.2908	0.3149	0.3581	0.4116	0.4480
Oceania	0.0743	0.1044	0.1493	0.2354	0.2512	0.2584
Globe	1.4760	1.8328	2.2772	2.7815	2.9720	3.1284

Note. The values for 1994–1998, 1999–2003, 2004–2008, and 2009–2013 are the mean for the corresponding 5-year period.

Amazon, Yangtze, Ob, Brahmaputra, and Irrawaddy Rivers (Figure 4). Besides these obvious increases along major rivers, the SLR also led to numerous new small methane-producing hotspots, which were scattered across the globe, and most of them were close to small streams (Figure 4). Noticeable geographic differences were observed in CH₄ flux intensity from this SLR-induced inundation extent: most CH₄ fluxes in tropical regions were higher than 100 g CH₄/m²/year, while they were low in northern high-latitude regions with a magnitude of smaller than 30 g CH₄/m²/year (Figure 4).

According to the simulation ($I_{no\ sea}$), 251 ± 18 Tg CH₄ was estimated to release to the atmosphere annually during the period of 1993–2014. Due to the 22-year SLR, global terrestrial ecosystems showed an increase of 3.13 Tg CH₄/year in their CH₄ emissions (Table 4). Although this amount only accounted for 1.2% of the global CH₄ emissions, it explained 17.3% of the mean annual variability during this period. At the continent level, Asia (largest) and Oceania (smallest) showed an increase of 1.13 and 0.26 Tg CH₄/year in CH₄ emissions in 2014 (Table 4). Although CH₄ emissions showed an overall increase under the SLR, the increase rate of CH₄ emissions did not show a linear response to the magnitude of increase in inundation extent. North America, for example, showed a notable increase in its inundation extent of 3.12 × 10⁴ km², or 25.8% of the global inundation extent increase (Table 2), but its increase in CH₄ emissions was relatively small at 0.35 Tg CH₄/year, only accounting for 11.2% of the total increase in CH₄ emissions (Table 4). Although Oceania only accounted for 4.6% of increase in global inundation extent, its high CH₄ production rates associated with high air temperatures contributed more than 8.3% of the global SLR-driven CH₄ emissions (Table 4). Temporally, we also found that the SLR resulted in more CH₄ emissions at the beginning

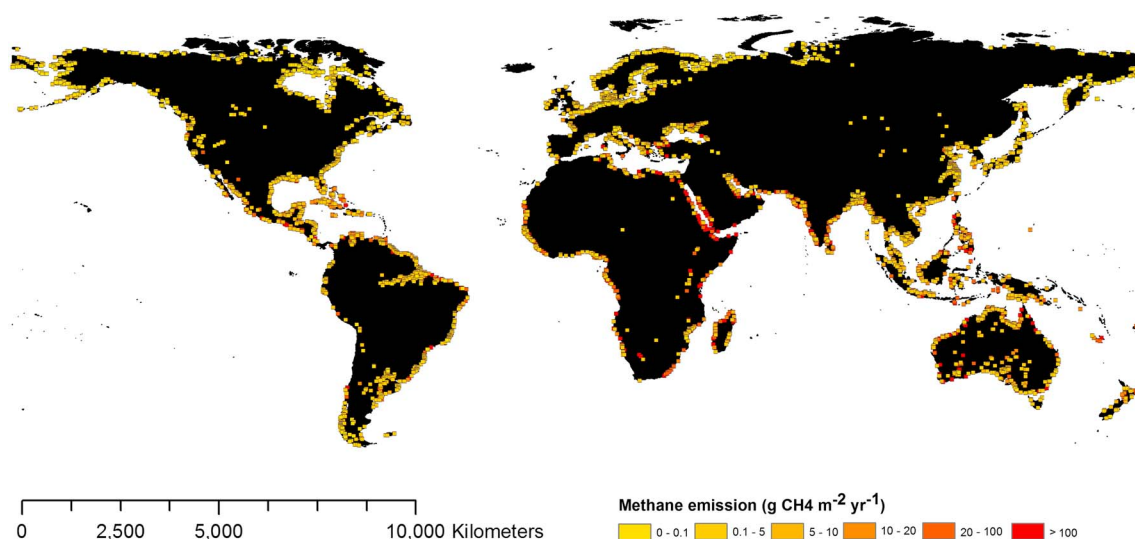


Figure 4. Increase in global methane emissions (g CH₄/m²/year) in 2014 due to sea-level rise. See details for selected main basins in Figure 5.

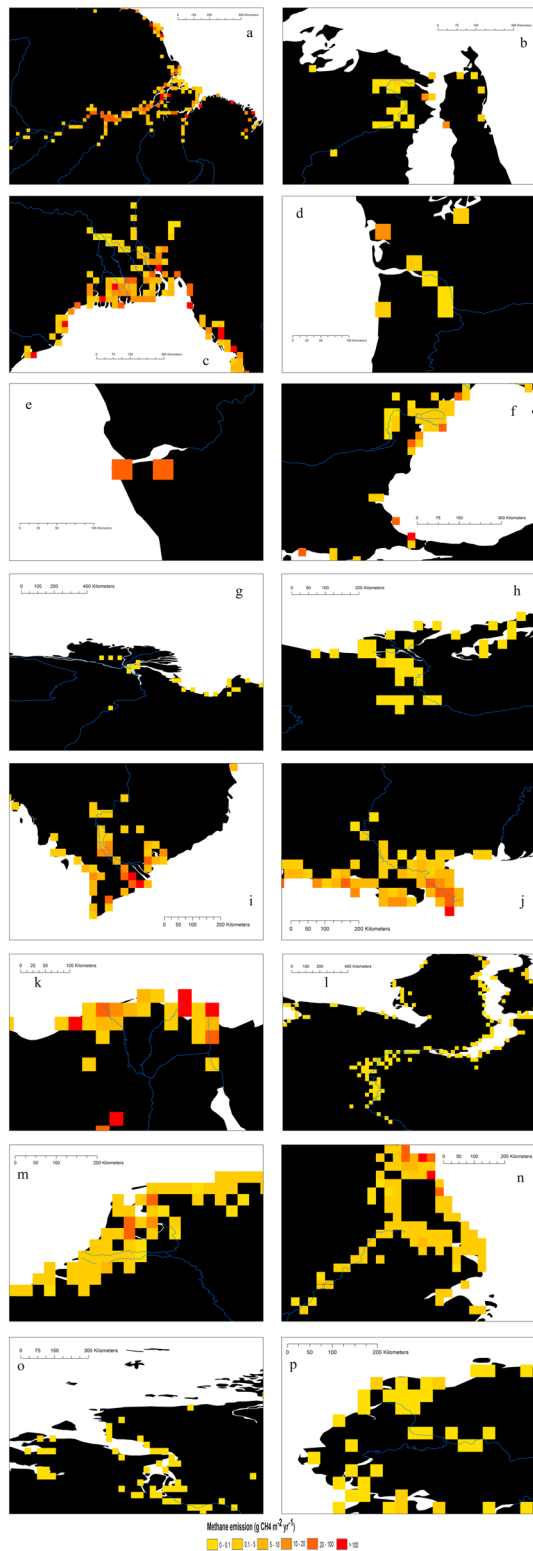


Figure 5. The increase in the methane emission ($\text{g CH}_4/\text{m}^2/\text{year}$) due to the sea-level rise in the selected major river basins in 2014: Amazon River (a), Amur River (b), Brahmaputra and Irrawaddy Rivers (c), Columbia River (d), Congo River (e), Danube River (f), Lena River (g), Mackenzie River (h), Mekong River (i), Mississippi River (j), Nile River (k), Ob River (l), Rhine River (m), Yangtze River (n), Yenisei River (o), and Yukon River (p).

of the study period: more than 50% increase in the CH_4 emissions occurred in the first 5 years in most of the continents (Table 4).

In all selected major basins, the SLR increased CH_4 emissions but with different magnitudes and spatial patterns (Figure 5 and Table 5). The spatial distribution of these increased CH_4 emissions at the basin-level largely followed the distribution of increases in inundation extent, indicating the important role of inundation extent in controlling CH_4 emissions. For example, the SLR resulted in new CH_4 source areas in the Amazon, Ob, Rhine, and Yangtze River basins, expanding hundreds of kilometers upstream from their outlets (Figures 5a, 5l, 5m, and 5n), which was consistent with the spatial distribution of their new inundation extent. Accordingly, the Columbia, Congo, and Mekong River basins showed the smallest increases in their CH_4 emissions owing to the smallest expansion in their inundation extent and most of them was close to rivers' outlets (Figures 5d, 5e, and 5i). Although the SLR caused some Arctic basins to have large increases in their inundation extent (Table 2), they usually had minor growth in their CH_4 emissions (Table 5). Most of new CH_4 source areas in the Lena, Mackenzie, Ob, Yenisei, and Yukon River basins only showed a low intensity of CH_4 emissions, ranging from 0 to $10 \text{ g CH}_4/\text{m}^2/\text{year}$ (Figures 5g, 5h, 5l, 5o, and 5p). The total increase in inundated area in the Lena, Mackenzie, Ob, Yenisei, and Yukon River basins accounted for 7.1% of the global increase (Table 2), while the increase in their CH_4 emissions only accounted for less than 0.02% of the global total (Table 5).

In addition to inundation extent, other environmental factors may also play roles in affecting CH_4 emissions in response to the SLR. Although the SLR led to considerable increases in inundation extent in most Arctic basins (Table 2), growth in their CH_4 emissions was very limited (Table 5). This discrepancy between inundation extent and CH_4 emissions in high-latitude regions (e.g., some Arctic basins) is mainly due to low temperature. Note that most new inundated area was characterized with extremely low air temperature which may significantly inhibit activity of methanogens. Moreover, CH_4 production is also limited by the availability of organic substrate; hence, more productive ecosystems tend to support stronger CH_4 emissions. For example, the Brahmaputra River basin showed almost twice the increase in its inundation extent than the Irrawaddy River basin (Table 2) and they had similar climate conditions. However, their increase in CH_4 emissions due to the SLR was similar (Table 5). It is worth noting that the dominant vegetation type in the delta of the Irrawaddy is mangrove forests, while that of the Brahmaputra basin is grass. The larger storage of soil carbon in mangrove forests (Thant et al., 2012; Webb et al., 2014) provides a greater substrate for methanogenesis compared to grass, resulting in a large difference in their CH_4 emissions. Another example showing the role of vegetation type is the comparison between Mississippi and Nile River basins. The increase in inundation extent of these two basins was similar (Table 2). Most of new flooded area in the Nile River basin was located in arid region with less organic substrates. In contrast, the Mississippi River has a large area of temperate forests in its outlet, resulting in 60% higher methane emissions after the 22-year SLR compared to the Nile River basin (Table 5).

Table 5
Annual and 5-Year Increase in CH₄ Emissions due to the Sea-Level Rise in the Selected Basins ($\times 10^{-5}$ Tg CH₄/year) and the Global (Tg CH₄/year) During 1993–2014

Basins	1993	1994–1998	1999–2003	2004–2008	2009–2013	2014
Amazon	835.4	1,572.1	2,057.2	2,488.8	2,753.3	2,839.3
Amur	1.8	21.6	64.4	92.6	86.4	103.6
Brahmaputra	28.7	151.7	315.4	442.1	478.5	682.0
Irrawaddy	92.8	242.2	274.3	261.5	292.6	278.6
Columbia	0.1	2.5	6.9	15.3	9.6	3.4
Congo	0.0	0.3	1.9	3.7	4.4	4.7
Danube	0.1	1.0	29.0	12.4	42.5	251.2
Lena	0.0	0.1	0.3	0.6	0.6	0.6
Mackenzie	0.0	0.1	0.4	0.8	0.9	1.0
Mekong	3.5	17.9	59.0	85.5	93.4	88.6
Mississippi	44.7	336.6	453.9	579.8	748.3	456.2
Nile	50.2	192.0	240.7	269.6	272.9	281.4
Ob	1.1	8.8	31.2	41.9	41.1	48.2
Rhine	230.3	575.3	743.8	792.7	979.9	1,206.5
Yangtze	17.9	434.9	563.6	695.1	827.3	807.3
Yenisei	0.0	0.2	1.0	2.4	2.5	3.1
Yukon	0.0	0.0	0.2	0.4	0.7	0.7
Globe	1.48	1.83	2.28	2.78	2.97	3.13

5. Conclusions

A surface water routing model was first coupled with a hydrological model to estimate changes in the inundated area by considering the local water balance and water horizontal transport in plains and rivers due to sea level rise. The improved hydrological model was then coupled with a methane model to analyze how CH₄ emissions respond to the changes in inundation extent at the global scale. We found that the mean annual MIE increased by more than 1.2×10^5 km² in the 22-year study period. Inundation extent increased nonlinearly with the sea-level rise due to different climatic conditions and geomorphic characteristics in various basins. Due to sea-level rise, annual CH₄ emissions increased by 3.13 Tg CH₄/year during 1993–2014 and most new CH₄ emission areas were located in outlets and riverside zones. In addition to inundated extent, changing soil temperature and vegetation type also play an important role in regulating methane emissions in response to the sea-level rise. Given that the current sea-level rise rate (3.3 mm/year) might be lower than that in a projected warming future, we expect that the future sea-level rise might play a more important role in affecting methane emissions.

This study can be improved in several aspects. First, the sea-level rise is assumed to increase by 3 mm/year across the globe. However, satellite altimetry measurements showed that the rate varies spatially (Archiving, Validation and Interpretation of Satellite Oceanographic data (AVISO), 2017). For example, the rate in the western Pacific is 3 times faster than the global mean since 1993. Thus, the global modeling could be improved by incorporating the spatial variability of the SLR. Moreover, the global sea-level rise may accelerate in response to future climate change (Pielke, 2008). Second, the effect of dams needs to be incorporated in future hydrological modeling as water level regulation may change hydraulic gradient at outlets, in turn, altering inundation extent. Third, previous studies (Jugold et al., 2012; Megonigal et al., 2008) also showed that CH₄ may be produced in oxic soils. With better understanding of this process, the inclusion of CH₄ emissions from unsaturated soils will contribute the CH₄ emission modeling due to the SLR. Finally, the coastlines could be inundated by seawater, in which sulfate plays an important role in regulating their CH₄ emissions. Many environmental factors such as air temperature, soil properties, geomorphic characteristics, vegetation types, and tide may also affect sulfate concentrations, in turn, affecting methane emissions from these saline inundated areas. A process-based methane biogeochemistry model for coastline saline wetlands and a substantial amount of methane cycling data shall improve future analysis of sea-level rise impacts on global methane emissions.

References

- Aviss, C., Weaver, A. J., & Meissner, K. J. (2011). Reduction in areal extent of high-latitude wetlands in response to permafrost thaw. *Nature Geoscience*, 4(7), 444–448. <https://doi.org/10.1038/ngeo1160>

Acknowledgments

We thank Dai Yamazaki for providing the CaMa-Flood code. The computing is supported by Rosen Center of High Performance Computing at Purdue. This research has been partly supported by a NASA project to Q. Z. (NNX17AK20G-1555205). The data presented in this study are available at <https://doi.org/10.5281/zenodo.1040370>. The data presented in this study can be obtained for free by request to D. W. Kicklighter at dkicklighter@mbl.edu.

- AVISO (2017). Archiving, validation and interpretation of satellite oceanographic data. Retrieved from www.aviso.oceanobs.com/
- Bates, P. D., Horritt, M. S., & Fewtrell, T. J. (2010). A simple inertial formulation of the shallow water equations for efficient two-dimensional flood inundation modelling. *Journal of Hydrology*, *387*(1-2), 33–45. <https://doi.org/10.1016/j.jhydrol.2010.03.027>
- Beven, K. J., & Kirkby, M. J. (1979). A physically based, variable contributing area model of basin hydrology. *Hydrological Sciences Bulletin*, *24*(1), 43–69. <https://doi.org/10.1080/02626667909491834>
- Bohn, T. J., Lettenmaier, D. P., Sathulur, K., Bowling, L. C., Podest, E., McDonald, K. C., & Friborg, T. (2007). Methane emissions from western Siberian wetlands: Heterogeneity and sensitivity to climate change. *Environmental Research Letters*, *2*(4), 9. <https://doi.org/10.1088/1748-9326/2/4/045015>
- Bohn, T. J., Melton, J. R., Ito, A., Kleinen, T., Spahni, R., Stocker, B. D., et al. (2015). WETCHIMP-WSL: Intercomparison of wetland methane emissions models over West Siberia. *Biogeosciences*, *12*(11), 3321–3349. <https://doi.org/10.5194/bg-12-3321-2015>
- Carter, A. J., & Scholes, R. J. (2000). SoilData v2.0: Generating a global database of soil properties, Council for Sci. and Ind. Res. Environ., Pretoria, South Africa.
- Cherkauer, K. A., Bowling, L. C., & Lettenmaier, D. P. (2003). Variable infiltration capacity cold land process model updates. *Global and Planetary Change*, *38*(1-2), 151–159. [https://doi.org/10.1016/S0921-8181\(03\)00025-0](https://doi.org/10.1016/S0921-8181(03)00025-0)
- Cherkauer, K. A., & Lettenmaier, D. P. (1999). Hydrologic effects of frozen soils in the upper Mississippi River basin. *Journal of Geophysical Research*, *104*(D16), 19,599–19,610. <https://doi.org/10.1029/1999JD900337>
- Church, J. A., & White, N. J. (2006). A 20th century acceleration in global sea-level rise. *Geophysical Research Letters*, *33*, L01602. <https://doi.org/10.1029/2005GL024826>
- Eliseev, A. V., Mokhov, I. I., Arzhanov, M. M., Demchenko, P. F., & Denisov, S. N. (2008). Interaction of the methane cycle and processes in wetland ecosystems in a climate model of intermediate complexity. *Izvestiya Atmospheric and Oceanic Physics*, *44*(2), 139–152. <https://doi.org/10.1134/s0001433808020011>
- Glagolev, M., Kleptsova, I., Filippov, I., Maksyutov, S., & Machida, T. (2011). Regional methane emission from West Siberia mire landscapes. *Environmental Research Letters*, *6*(4), 7. <https://doi.org/10.1088/1748-9326/6/4/045214>
- Hansen, M. C., Defries, R. S., Townshend, J. R. G., & Sohlberg, R. (2000). Global land cover classification at 1 km spatial resolution using a classification tree approach. *International Journal of Remote Sensing*, *21*(6–7), 1331–1364. <https://doi.org/10.1080/014311600210209>
- Hodson, E. L., Poulter, B., Zimmermann, N. E., Prigent, C., & Kaplan, J. O. (2011). The El Niño–Southern Oscillation and wetland methane interannual variability. *Geophysical Research Letters*, *38*, L08810. <https://doi.org/10.1029/2011GL046861>
- Hopcroft, P. O., Valdes, P. J., & Beerling, D. J. (2011). Simulating idealized Dansgaard-Oeschger events and their potential impacts on the global methane cycle. *Quaternary Science Reviews*, *30*(23–24), 3258–3268. <https://doi.org/10.1016/j.quascirev.2011.08.012>
- Jugold, A., Althoff, F., Hurkuck, M., Greule, M., Lenhart, K., Lelieveld, J., & Keppler, F. (2012). Non-microbial methane formation in oxic soils. *Biogeosciences*, *9*, 5291–5301. <https://doi.org/10.5194/bgd-9-11961-2012>
- Kalnay, E., Kanamitsu, M., Kistler, R., Collins, W., Deaven, D., Gandin, L., et al. (1996). The NCEP/NCAR 40-year reanalysis project. *Bulletin of the American Meteorological Society*, *77*(3), 437–471. [https://doi.org/10.1175/1520-0477\(1996\)077%3C0437:tnyrp%3E2.0.co;2](https://doi.org/10.1175/1520-0477(1996)077%3C0437:tnyrp%3E2.0.co;2)
- Kim, H., Yeh, P. J. F., Oki, T., & Kanae, S. (2009). Role of rivers in the seasonal variations of terrestrial water storage over global basins. *Geophysical Research Letters*, *36*, L17402. <https://doi.org/10.1029/2009GL039006>
- Liang, X., Lettenmaier, D. P., Wood, E. F., & Burges, S. J. (1994). A simple hydrologically based model of land surface water and energy fluxes for GSIms. *Journal of Geophysical Research*, *99*, 14,415–14,428. <https://doi.org/10.1029/94JD00483>
- Lu, X. L., & Zhuang, Q. L. (2012). Modeling methane emissions from the Alaskan Yukon River basin, 1986–2005, by coupling a large-scale hydrological model and a process-based methane model. *Journal of Geophysical Research*, *117*, G02010. <https://doi.org/10.1029/2011JG001843>
- Lu, X. L., Zhuang, Q. L., Liu, Y. L., Zhou, Y. Y., & Aghakouchak, A. (2016). A large-scale methane model by incorporating the surface water transport. *Journal of Geophysical Research: Biogeosciences*, *121*, 1657–1674. <https://doi.org/10.1002/2016jg003321>
- Megonigal, J. P., & Guenther, A. B. (2008). Methane emissions from upland forest soils and vegetation. *Tree Physiology*, *28*, 491–498. <https://doi.org/10.1093/treephys/28.4.491>
- Melillo, J. M., McGuire, A. D., Kicklighter, D. W., Moore, B. III, Vörösmarty, C. J., & Schloss, A. L. (1993). Global climate change and terrestrial net primary production. *Nature*, *363*(6426), 234–240. <https://doi.org/10.1038/363234a0>
- Melton, J. R., Wania, R., Hodson, E. L., Poulter, B., Ringeval, B., Spahni, R., et al. (2013). Present state of global wetland extent and wetland methane modelling: Conclusions from a model inter-comparison project (WETCHIMP). *Biogeosciences*, *10*(2), 753–788. <https://doi.org/10.5194/bg-10-753-2013>
- Merrifield, M. A., Merrifield, S. T., & Mitchum, G. T. (2009). An anomalous recent acceleration of global sea level rise. *Journal of Climate*, *22*(21), 5772–5781. <https://doi.org/10.1175/2009jcli2985.1>
- Nicholls, R. J., & Cazenave, A. (2010). Sea-level rise and its impact on coastal zones. *Science*, *328*(5985), 1517–1520. <https://doi.org/10.1126/science.1185782>
- Nijssen, B., Schnur, R., & Lettenmaier, D. P. (2001). Global retrospective estimation of soil moisture using the variable infiltration capacity land surface model, 1980–93. *Journal of Climate*, *14*(8), 1790–1808. [https://doi.org/10.1175/1520-0442\(2001\)014%3C1790:greosm%3E2.0.co;2](https://doi.org/10.1175/1520-0442(2001)014%3C1790:greosm%3E2.0.co;2)
- Papa, F., Prigent, C., Aires, F., Jimenez, C., Rossow, W. B., & Matthews, E. (2010). Interannual variability of surface water extent at the global scale, 1993–2004. *Journal of Geophysical Research*, *115*, D12111. <https://doi.org/10.1029/2009JD012674>
- Pickett-Heaps, C. A., Jacob, D. J., Wecht, K. J., Kort, E. A., Wofsy, S. C., Diskin, G. S., et al. (2011). Magnitude and seasonality of wetland methane emissions from the Hudson Bay Lowlands (Canada). *Atmospheric Chemistry and Physics*, *11*(8), 3773–3779. <https://doi.org/10.5194/acp-11-3773-2011>
- Pielke, R. A. (2008). Climate predictions and observations. *Nature Geoscience*, *1*(4), 206. <https://doi.org/10.1038/ngeo157>
- Prigent, C., Papa, F., Aires, F., Rossow, W. B., & Matthews, E. (2007). Global inundation dynamics inferred from multiple satellite observations, 1993–2000. *Journal of Geophysical Research*, *112*, D12107. <https://doi.org/10.1029/2006JD007847>
- Riley, W. J., Subin, Z. M., Lawrence, D. M., Swenson, S. C., Torn, M. S., Meng, L., et al. (2011). Barriers to predicting changes in global terrestrial methane fluxes: Analyses using CLM4Me, a methane biogeochemistry model integrated in CESM. *Biogeosciences*, *8*(7), 1925–1953. <https://doi.org/10.5194/bg-8-1925-2011>
- Ringeval, B., Decharme, B., Piao, S. L., Ciais, P., Papa, F., de Noblet-Ducoudré, N., et al. (2012). Modelling sub-grid wetland in the ORCHIDEE global land surface model: Evaluation against river discharges and remotely sensed data. *Geoscientific Model Development*, *5*(4), 941–962. <https://doi.org/10.5194/gmd-5-941-2012>
- Ringeval, B., Friedlingstein, P., Koven, C., Ciais, P., de Noblet-Ducoudré, N., Decharme, B., & Cadule, P. (2011). Climate-CH₄ feedback from wetlands and its interaction with the climate-CO₂ feedback. *Biogeosciences*, *8*(8), 2137–2157. <https://doi.org/10.5194/bg-8-2137-2011>

- Running, S. W., & Zhao, M. (2015). Daily GPP and annual NPP (MOD17A2/A3) products NASA Earth Observing System MODIS land algorithm. MOD17 User's Guide (28 pp.).
- Schroeder, R., McDonald, K. C., Chapman, B. D., Jensen, K., Podest, E., Tessler, Z. D., et al. (2015). Development and evaluation of a multi-year fractional surface water data set derived from active/passive microwave remote sensing data. *Remote Sensing*, 7, 16,688–16,732. <https://doi.org/10.3390/rs71215843>
- Schroeder, R., Rawlins, M. A., McDonald, K. C., Podest, E., Zimmermann, R., & Kueppers, M. (2010). Satellite microwave remote sensing of North Eurasian inundation dynamics: Development of coarse-resolution products and comparison with high-resolution synthetic aperture radar data. *Environmental Research Letters*, 5(1), 015003. <https://doi.org/10.1088/1748-9326/5/1/015003>
- Singarayer, J. S., Valdes, P. J., Friedlingstein, P., Nelson, S., & Beerling, D. J. (2011). Late Holocene methane rise caused by orbitally controlled increase in tropical sources. *Nature*, 470(7332), 82–85. <https://doi.org/10.1038/nature09739>
- Spahni, R., Wania, R., Neef, L., van Weele, M., Pison, I., Bousquet, P., et al. (2011). Constraining global methane emissions and uptake by ecosystems. *Biogeosciences*, 8(6), 1643–1665. <https://doi.org/10.5194/bg-8-1643-2011>
- Thant, Y. M., Kanzaki, M., Ohta, S., & Than, M. M. (2012). Carbon sequestration by mangrove plantations and a natural regeneration stand in the Ayeyarwady Delta, Myanmar. *Tropics*, 21, 1–10.
- Tian, H. Q., Xu, X. F., Lu, C. Q., Liu, M. L., Ren, W., Chen, G. S., et al. (2011). Net exchanges of CO₂, CH₄, and N₂O between China's terrestrial ecosystems and the atmosphere and their contributions to global climate warming. *Journal of Geophysical Research*, 116, G02011. <https://doi.org/10.1029/2010JG001393>
- Wania, R., Ross, I., & Prentice, I. C. (2010). Implementation and evaluation of a new methane model within a dynamic global vegetation model: LPJ-WHyMe v1.3.1. *Geoscientific Model Development*, 3(2), 565–584. <https://doi.org/10.5194/gmd-3-565-2010>
- Webb, E. L., Jachowski, N. R. A., Phelps, J., Friess, D. A., Than, M. M., & Ziegler, A. D. (2014). Deforestation in the Ayeyarwady delta and the conservation implications of an internationally-engaged Myanmar. *Global Environmental Change*, 24, 321–333. <https://doi.org/10.1016/j.gloenvcha.2013.10.007>
- Winderlich, J., Chen, H., Gerbig, C., Seifert, T., Kolle, O., Lavric, J. V., et al. (2010). Continuous low-maintenance CO₂/CH₄/H₂O measurements at the Zotino Tall Tower Observatory (ZOTTO) in Central Siberia. *Atmospheric Measurement Techniques*, 3(4), 1113–1128. <https://doi.org/10.5194/amt-3-1113-2010>
- Worthy, D. E. J., Levin, I., Hopper, F., Ernst, M. K., & Trivett, N. B. A. (2000). Evidence for a link between climate and northern wetland methane emissions. *Journal of Geophysical Research*, 105(D3), 4031–4038. <https://doi.org/10.1029/1999JD901100>
- Xu, X. F., & Tian, H. Q. (2012). Methane exchange between marshland and the atmosphere over China during 1949–2008. *Global Biogeochemical Cycles*, 26, GB2006. <https://doi.org/10.1029/2010GB003946>
- Yamazaki, D., Baugh, C. A., Bates, P. D., Kanae, S., Alsdorf, D. E., & Oki, T. (2012). Adjustment of a spaceborne DEM for use in floodplain hydrodynamic modeling. *Journal of Hydrology*, 436–437, 81–91. <https://doi.org/10.1016/j.jhydrol.2012.02.045>
- Yamazaki, D., Kanae, S., Kim, H., & Oki, T. (2011). A physically based description of floodplain inundation dynamics in a global river routing model. *Water Resources Research*, 47, W04501. <https://doi.org/10.1029/2010WR009726>
- Yamazaki, D., Lee, H., Alsdorf, D. E., Dutra, E., Kim, H., Kanae, S., & Oki, T. (2012). Analysis of the water level dynamics simulated by a global river model: A case study in the Amazon River. *Water Resources Research*, 48, W09508. <https://doi.org/10.1029/2012WR011869>
- Yamazaki, D., Oki, T., & Kanae, S. (2009). Deriving a global river network map and its sub-grid topographic characteristics from a fine-resolution flow direction map. *Hydrology and Earth System Sciences*, 13(11), 2241–2251. <https://doi.org/10.5194/hess-13-2241-2009>
- Yamazaki, D., O'Loughlin, F., Trigg, M. A., Miller, Z. F., Pavelsky, T. M., & Bates, P. D. (2014). Development of the global width database for large rivers. *Water Resources Research*, 50, 3467–3480. <https://doi.org/10.1002/2013wr014664>
- Zhuang, Q., McGuire, J. M., Clein, J. S., Dargaville, R. J., Kicklighter, D. W., Myneni, R. B., et al. (2003). Carbon cycling in extratropical terrestrial ecosystems of the Northern Hemisphere during the 20th century: A modeling analysis of the influences of soil thermal dynamics. *Tellus Series B: Chemical and Physical Meteorology*, 55(3), 751–776. <https://doi.org/10.1034/j.1600-0889.2003.00060.x>
- Zhuang, Q., Melillo, J. M., Kicklighter, D. W., Prinn, R. G., McGuire, A. D., Steudler, P. A., et al. (2004). Methane fluxes between terrestrial ecosystems and the atmosphere at northern high latitudes during the past century: A retrospective analysis with a process-based biogeochemistry model. *Global Biogeochemical Cycles*, 18, GB3010. <https://doi.org/10.1029/2004GB002239>